

Efficient Modeling of Quasi-Periodic Data with Seasonal Gaussian Process

Ziang Zhang

Department of Statistical Sciences, University of Toronto
and

Patrick Brown

Department of Statistical Sciences, University of Toronto
Centre for Global Health Research, St Michael's Hospital
and

Jamie Stafford

Department of Statistical Sciences, University of Toronto

May 18, 2023

Abstract

Quasi-periodicity refers to a pattern in a function where it appears periodic but has evolving amplitudes over time. This is often the case in practical settings such as the modeling of case counts of infectious disease or the carbon dioxide (CO₂) concentration over time. In this paper, we introduce a class of Gaussian processes, called seasonal Gaussian Processes (sGP), for model-based inference of such quasi-periodic behavior. We illustrate that the exact sGP can be efficiently fit within $O(n)$ time using its state space representation for equally spaced locations. However, for large datasets with irregular spacing, the exact approach becomes computationally inefficient and unstable. To address this, we develop a continuous finite dimensional approximation for sGP using the seasonal B-spline (sB-spline) basis constructed by damping B-splines with sinusoidal functions. We prove that the proposed approximation converges in distribution to the true sGP as the number of basis functions increases, and show its superior approximation quality through numerical studies. We also provide a unified and interpretable way to define priors for the sGP, based on the notion of predictive standard deviation (PSD). Finally, we implement the proposed inference method on several real data examples to illustrate its practical usage.

Keywords: Hierarchical Model, Bayesian Methods, Statistical Computing, Prior Elicitation

1. Introduction

In astronomical studies the brightness of Sun-like stars tends to exhibit seasonal variation with amplitudes evolving overtime owing to the rotational modulation of magnetically active regions (Roberts et al., 2013). This kind of quasi-periodic behavior can also be observed in the weekly mortality counts due to influenza, and the carbon dioxide concentration (CO₂) readings at the Mauna Loa observatory (Rasmussen, 2003). Therefore, inferring an unknown function g with quasi-periodic behavior is often a crucial task in a variety of contexts.

In this paper, we proposed a class of Gaussian processes (\mathcal{GP}), which we call seasonal Gaussian Processes (sGP), to make inference of a quasi-periodic function g . The sGP has a natural construction through an ordinary stochastic differential equation (SDE) which provides a clear interpretation of the degree of quasi-periodicity in the inferred function. Additionally, once written into a state space representation with its first derivative, the sGP has a Markov property that simplifies the computation for inference at equally spaced locations.

However, for large datasets with irregular spacing, the exact approach can become computationally inefficient and numerically unstable. To address this, we develop a novel finite dimensional continuous approximation to the sGP with the seasonal B-spline basis (sB-spline). Motivated by the covariance structure of the sGP, sB-splines are constructed by damping B-splines with sinusoidal functions. The proposed sB-spline approximation is then constructed using the finite element method (FEM)(Brenner et al., 2008) in a strategy similar to Lindgren and Rue (2008), Lindgren et al. (2011) and Zhang et al. (2023b) for approximating different classes of Gaussian processes. Improvements in computational efficiency are realized by adopting a least squares approach so the resulting approximation is fully determined by a set of basis weights with a highly sparse precision matrix. This approximation is shown to converge rapidly to the true sGP as the number of basis functions increases.

The remainder of the paper is organized as follows. In Section 2, we introduce the sGP model and its SDE characterization. We then derive some useful properties of the sGP, in particular a state-space representation which makes the sGP ideal for inference. In Section 3.1, we develop our proposed sB-spline approximation to the sGP using the FEM. We also discuss the computational and theoretical properties

that justify its practical advantages. In Section 4, we derive the predictive standard deviation (PSD) of the sGP (Zhang et al., 2023b), and use it to define prior for the standard deviation parameter of the sGP in a unified and interpretable way. In Section 5, we demonstrate the effectiveness and versatility of our proposed methodology for inferring quasi-periodic functions. We first apply the approach to three simple examples as a proof of concept, and then showcase its advantage by re-analyzing the atmospheric Carbon Dioxide (CO₂) concentrations data collected in Hawaii, which was originally analyzed in Rust et al. (1979). Our inference uses the posterior approximation algorithm in Stringer et al. (2022); Bilodeau et al. (2022). For a more detailed description of how to implement this algorithm with \mathcal{GP} , one can refer to Section 3 in Zhang et al. (2023b).

2. Inference with the Seasonal Gaussian Process

We consider the following hierarchical model:

$$\begin{aligned}
 Y_i | \boldsymbol{\eta} &\stackrel{\text{ind}}{\sim} \pi(Y_i | \boldsymbol{\eta}, \kappa), \\
 \eta_i &= \mathbf{v}_i^T \boldsymbol{\beta} + \sum_{l=1}^L g_l(x_{li}), \\
 g_l : \Omega_l &\rightarrow \mathbb{R}, \quad g_l \stackrel{\text{ind}}{\sim} \mathcal{GP}(C_l), \forall l \in [L].
 \end{aligned} \tag{1}$$

Here $\pi(Y_i | \boldsymbol{\eta}, \kappa)$ is a twice continuously-differentiable density with linear predictors $\boldsymbol{\eta} = [\eta_1, \dots, \eta_n]^T$, covariates \mathbf{v}_i , x_{li} and hyperparameter κ . Each unknown function g_l is assigned an independent Gaussian Process (\mathcal{GP}) model with zero mean and covariance function C_l . The model 1 is termed the Extended Latent Gaussian Model in Stringer et al. (2022), and an example is the partial likelihood of Cox proportional hazards model where each Y_i depends on multiple elements of $\boldsymbol{\eta}$ (Zhang et al., 2023a). For the purpose of exposition, we consider the inference of a single unknown function g with the sGP in the remainder of this section as well as Section 3 and Section 4.

2.1. Seasonal Gaussian Process: A Differential Equation Characterization

The seasonal Gaussian process (sGP) is a zero-mean \mathcal{GP} defined for functions that exhibit quasi-periodic behavior. It is characterized by two parameters, the frequency parameter $\alpha \in \mathbb{R}^+$ and the standard

deviation (SD) parameter $\sigma \in \mathbb{R}^+$. If the function g is assigned the sGP model, which we denote as $g \sim \text{sGP}(\alpha, \sigma)$, then g satisfies the following stochastic differential equation (SDE):

$$Lg(x) = \left[\frac{d^2}{dx^2} + \alpha^2 \right] g(x) = \sigma \xi(x), \quad (2)$$

where $\xi(x)$ is the Gaussian white noise process. Note that the null space of the SDE in Eq. (2) is:

$$\text{Null}\{L\} = \text{span}\{\cos(\alpha x), \sin(\alpha x)\}, \quad (3)$$

which is the space of sinusoidal functions with period $2\pi/\alpha$. For identifiability, we define the sGP g in Eq. (2) to satisfy the following initial conditions

$$g(0) = g'(0) = 0, \quad (4)$$

without the loss of generality. More general initial conditions can be accommodated by adding two global trigonometric functions $\{v_1 \cos(\alpha x), v_2 \sin(\alpha x)\}$ to g , where initial conditions become $g(0) = v_1$ and $g'(0) = v_2 \alpha$.

The sGP model has a direct interpretation in its parameters: α specifies the frequency and the periodicity of the function g , and σ specifies the degree that g could deviate from the sinusoidal space in Eq. (3). When σ is larger, the sample path of sGP can deviate more from the sinusoidal pattern, which allows for more quasi-periodic behavior in the inferred g . Therefore, the quasi-periodic behavior of g such as in the sunspot variation could be accommodated and quantified by the sGP model.

2.2. Properties of the Seasonal Gaussian Process

The specific covariance function of the sGP model in Eq. (2) is given in Proposition 1.

Proposition 1 (Covariance Function of the Seasonal Gaussian Process). *Let $g \sim \text{sGP}(\alpha, \sigma)$. Then g has*

a covariance function:

$$\begin{aligned} C(x_1, x_2) &= \left(\frac{\sigma}{\alpha}\right)^2 \left[\frac{x_1}{2} \cos(\alpha(x_2 - x_1)) - \frac{\cos(\alpha x_2) \sin(\alpha x_1)}{2\alpha} \right] \\ &= \left(\frac{\sigma}{\alpha}\right)^2 \left[\frac{\cos(\alpha x_2) x_1}{2} \cos(\alpha x_1) + \left(\frac{\sin(\alpha x_2) x_1}{2} - \frac{\cos(\alpha x_2)}{2\alpha} \right) \sin(\alpha x_1) \right], \end{aligned} \quad (5)$$

for any $x_1, x_2 \in \mathbb{R}^+$ such that $x_1 \leq x_2$.

The detailed derivation of Proposition 1 is provided in Appendix A. Since the covariance function in Eq. (5) has the form of damped sinusoidal waves, it is clear that the sGP should be viewed as a model for quasi-periodic functions. As an illustration, some simulated sample paths from the sGP models with different α are shown in Fig. 1.

Another property that makes sGP convenient to use in practice is that when augmented with its first derivative, the resulting augmented model has a state space representation that satisfies the Markov property. This property is summarized in Theorem 1.

Theorem 1 (State Space Representation of the sGP). *Consider $g \sim sGP(\alpha, \sigma)$, and let $\mathbf{s} = \{s_1, \dots, s_n\} \subset \mathbb{R}^+$ denotes a set of n sorted locations and spacing $d_1 = s_1$ and $d_i = s_i - s_{i-1}$ for $i \in \{2, \dots, n\}$. Then the augmented vector $\mathbf{g}_{aug}(s_i) = [g(s_i), g'(s_i)]^T$ can be written as a Markov model:*

$$\mathbf{g}_{aug}(s_{i+1}) = \mathbf{R}_{i+1} \mathbf{g}_{aug}(s_i) + \boldsymbol{\epsilon}_{i+1}, \quad (6)$$

where $\boldsymbol{\epsilon}_i \stackrel{ind}{\sim} N(0, \boldsymbol{\Sigma}_i)$. The 2×2 matrices \mathbf{R}_i and $\boldsymbol{\Sigma}_i = \mathbf{Q}_i^{-1}$ are respectively defined as:

$$\mathbf{R}_i = \begin{bmatrix} \cos(\alpha d_i) & \frac{1}{\alpha} \sin(\alpha d_i) \\ -\alpha \sin(\alpha d_i) & \cos(\alpha d_i) \end{bmatrix}, \quad \boldsymbol{\Sigma}_i = \sigma^2 \begin{bmatrix} \frac{1}{\alpha^2} \left(\frac{d_i}{2} - \frac{\sin(2\alpha d_i)}{4\alpha} \right) & \frac{\sin^2(\alpha d_i)}{2\alpha^2} \\ \frac{\sin^2(\alpha d_i)}{2\alpha^2} & \frac{2\alpha d_i + \sin(2\alpha d_i)}{4\alpha} \end{bmatrix}. \quad (7)$$

A proof of theorem 1 can be found in Appendix B. An implication of Theorem 1 is that the discretely observed sGP model can be fitted sequentially using a filtering method by augmenting the state space with first derivatives. This is particularly useful when the response variable y is Gaussian, as demonstrated by Ansley and Kohn (1990) and Ansley et al. (1993). Another implication of Theorem 1 is that unlike $[g(s_1), \dots, g(s_n)]^T \in \mathbb{R}^n$ which has a dense precision matrix, the augmented vector

where $\mathbf{Q}_i = \mathbf{\Sigma}_i^{-1}$, $\mathbf{A}_i = \mathbf{R}_i^T \mathbf{Q}_i \mathbf{R}_i$ and $\mathbf{H}_i = -\mathbf{R}_i^T \mathbf{Q}_i$.

When all the locations are equally spaced, the Markov model (1) is reduced to a first-order vector auto-regression (VAR) model which requires only one coefficient matrix \mathbf{R} and one error covariance $\mathbf{\Sigma}$ to be computed in order to obtain the entire precision matrix \mathbf{Q}_{aug} . Because of the sparse structure of \mathbf{Q}_{aug} , the entire augmented vector $[\mathbf{g}_{aug}(s_1)^T, \dots, \mathbf{g}_{aug}(s_n)^T]^T$ can then be efficiently incorporated into the modern approximate Bayesian inference methods of Stringer et al. (2022); Rue et al. (2009). For large and irregularly spaced datasets, however, the approach using the state-space representation becomes computationally challenging, in particular when the correlation is strong. This is because of the need to compute and invert each matrix $\mathbf{\Sigma}_i$ in Eq. (8). It is therefore often useful to consider a continuous finite-dimensional approximation to the entire process, which we introduce in the following section.

3. Finite Dimensional Approximation to SGP

In this section, we derive the proposed seasonal B-spline (sB-spline) approximation as a Least Square approximation through the Finite Element Method (FEM). Our results demonstrate that this approximation has both desirable computational and theoretical properties. In Section 3.1, we provide the context and a general form of the FEM approximation. For the purpose of computation efficiency, we then adopt a least square approach to construct the FEM approximation and choose the cubic B-spline functions as the basis in Section 3.2. In Section 3.3, we improve the FEM approximation by damping the basis functions with sinusoidal functions, which finally yields our proposed sB-spline approximation.

3.1. Finite Element Method

Given $\Omega = [a, b]$ for some $a, b \in \mathbb{R}^+$, the idea of FEM is to construct an approximation \tilde{g}_k that has the form of:

$$\tilde{g}_k(x) = \sum_{i=1}^k w_i \varphi_i(x), \quad (9)$$

where $\mathbf{w} = (w_1, \dots, w_k)^T \in \mathbb{R}^k$ is a set of random weights and $\mathbb{B}_k = \{\varphi_i(x), i \in [k]\}$ is a set of k predetermined basis functions. Given a set of test functions $\mathbb{T}_k = \{\phi_i(x); i \in [k]\}$, the distribution of the unknown

weight vector \mathbf{w} is defined such that

$$\begin{aligned}\langle L\tilde{g}_k(x), \phi_i(x) \rangle &\stackrel{d}{=} \sigma \langle Lg(x), \phi_i(x) \rangle \\ &= \sigma \langle \xi(x), \phi_i(x) \rangle,\end{aligned}\tag{10}$$

for any test function $\phi_i \in \mathbb{T}_k$, where $\langle f_1(x), f_2(x) \rangle := \int_{\Omega} f_1(x)f_2(x)dx$ denotes inner-product between any $f_1, f_2 \in L^2$. The requirement Eq. (10) can be vectorized as

$$\mathbf{B}\mathbf{w} \stackrel{d}{=} N(\mathbf{0}, \sigma^2\mathbf{T}),\tag{11}$$

where \mathbf{B} and \mathbf{T} are $k \times k$ matrices with entries:

$$\mathbf{B}_{ij} = \langle \phi_i(x), L\varphi_j(x) \rangle, \quad \mathbf{T}_{ij} = \langle \phi_i(x), \phi_j(x) \rangle.\tag{12}$$

When both \mathbf{B} and \mathbf{T} are non-singular, the requirement in Eq. (10) implies $\mathbf{w} \sim N(\mathbf{0}, \sigma^2\boldsymbol{\Sigma}_{\mathbf{w}})$ where the precision matrix $\boldsymbol{\Sigma}_{\mathbf{w}}^{-1} = \mathbf{B}^T\mathbf{T}^{-1}\mathbf{B}$.

3.2. Least Square Approximation with Cubic B-Spline Basis

Given a set of locations \mathbf{s} , the FEM approximation at these locations can be written as $\tilde{\mathbf{g}}_k(\mathbf{s}) = \boldsymbol{\Phi}\mathbf{w}$ where $\boldsymbol{\Phi}$ is $n \times k$ design matrix with ij element $\boldsymbol{\Phi}_{ij} = \varphi_j(s_i)$. The computational bottleneck of the above FEM approximation therefore depends on both $\boldsymbol{\Sigma}_{\mathbf{w}}^{-1}$ and $\boldsymbol{\Phi}$. We aim to find a FEM approximation such that both $\boldsymbol{\Sigma}_{\mathbf{w}}^{-1}$ and $\boldsymbol{\Phi}$ can be computed efficiently and have sparse structures.

To simplify the computation of the precision matrix $\boldsymbol{\Sigma}_{\mathbf{w}}^{-1}$, we consider a least square approach to construct the FEM approximation, which corresponds to setting the test function $\phi_i(x) = L\varphi_i(x)$ for each $i \in [k]$. This strategy reduces the precision matrix to $\boldsymbol{\Sigma}_{\mathbf{w}}^{-1} = \mathbf{T}^T\mathbf{T}^{-1}\mathbf{T} = \mathbf{T}$, and hence avoids the need to compute another matrix \mathbf{B} or to invert the matrix \mathbf{T} (Zhang et al., 2023b).

It remains to choose a set of basis functions \mathbb{B}_k such that the corresponding matrices \mathbf{T} and $\boldsymbol{\Phi}$ are sparse. Given any basis \mathbb{B}_k , it can be shown that the precision matrix \mathbf{T} can be computed as:

$$\mathbf{T} = a^4\mathbf{G} + \mathbf{C} + a^2\mathbf{M},\tag{13}$$

with $\mathbf{G}_{ij} = \langle \varphi_i, \varphi_j \rangle$, $\mathbf{C}_{ij} = \langle \frac{d^2 \varphi_i}{dx^2}, \frac{d^2 \varphi_j}{dx^2} \rangle$ and $\mathbf{M}_{ij} = \langle \varphi_i, \frac{d^2 \varphi_j}{dx^2} \rangle + \langle \frac{d^2 \varphi_i}{dx^2}, \varphi_j \rangle$. The detailed derivation is provided in Appendix C. Given Eq. (13), it is natural to consider using the cubic B-spline basis as \mathbb{B}_k in the approximation, which ensures the sparsity of \mathbf{T} with $O(8k)$ nonzero elements, and the sparsity of Φ with $O(4k)$ nonzero elements (de Boor, 2000). The cubic B-spline basis yields a computationally efficient approximation to the true sGP. Furthermore, the following Theorem 2 guarantees the convergence of the approximation to the true sGP process as the number of basis k increases.

Theorem 2 (Convergence of B-spline Approximation). *Let $\Omega = [a, b]$ where $a, b \in \mathbb{R}^+$ and let $g \sim \text{sGP}(\alpha, \sigma)$. Assume \mathbb{B}_k is a set of k cubic B-splines constructed with equally spaced knots over Ω , and \tilde{g}_k denotes the corresponding FEM approximation defined as in Eq. (9), then:*

$$\lim_{k \rightarrow \infty} \mathcal{C}_k(x_1, x_2) = \mathcal{C}(x_1, x_2),$$

for any $x_1, x_2 \in \Omega$, where $\mathcal{C}(x_1, x_2) = \text{Cov}[g(x_1), g(x_2)]$, $\mathcal{C}_k(x_1, x_2) = \text{Cov}[\tilde{g}_k(x_1), \tilde{g}_k(x_2)]$.

The proof of this theorem is provided in Appendix D.

3.3. Improving Approximation Accuracy with sB-Spline

Although Theorem 2 guarantees the limiting property of the cubic B-spline approximation, the error from the cubic B-spline approximation could be non-negligible when only a limited number of basis is used, which is a typical situation in real applications. To see that, note the covariance function (5) at a fixed location x_1 can be written as:

$$C_{x_1}(x) = C(x_1, x) = l_{x_1}(x) \cos(\alpha x) + \tilde{l}_{x_1}(x) \sin(\alpha x), \quad (14)$$

where $l_{x_1}(x)$ and $\tilde{l}_{x_1}(x)$ are piecewise linear functions with a single knot at x_1 . In order to accurately approximate the distribution of the original sGP, the basis \mathbb{B}_k needs to be flexible enough to approximate well the covariance function $C_{x_1}(x)$ for any $x_1 \in \Omega$. The cubic B-spline basis can well approximate the covariance function when α is small relative to the width of Ω . However, when α is large relative to the width of Ω , the covariance function will be too oscillating to be approximated well by the cubic B-spline basis. See Fig. 2 for example.

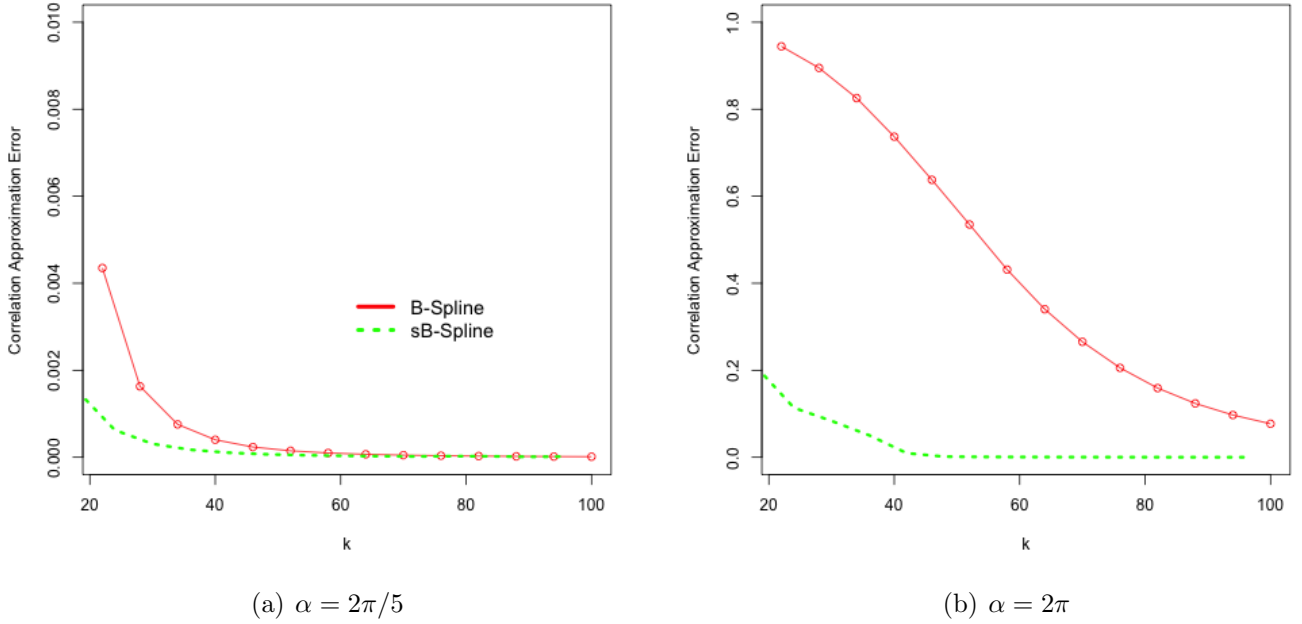


Figure 2: Assessing the approximation accuracy with cubic B-spline (red) and sB-spline (green) basis. In order to make the y-axis comparable, we focus on the correlation function $\rho_5(x)$ instead of the covariance function. The y-axis shows the maximum correlation approximation error $|\rho_5(x) - \tilde{\rho}_5(x)|$ for $x \in [1, 9]$, where $\rho_5(x) = \text{Corr}[g(5), g(x)]$ and $\tilde{\rho}_5(x) = \text{Corr}[\tilde{g}_k(5), \tilde{g}_k(x)]$ are respectively the correlation functions of the true sGP and of the approximation. The interval $\Omega = [0, 10]$, $\sigma = 1$ and $\alpha = 2\pi$ or $2\pi/5$.

Given $C_{x_1}(x)$ is itself a piece-wise polynomial damped by sinusoidal functions, we increase the accuracy of our approximation by augmenting the B-spline basis with B-splines that are also damped by sinusoidal functions. We call this new basis the seasonal B-spline (*sB-spline*) basis. The detailed construction of the sB-spline is given as the following. We first construct $r \in \mathbb{Z}^+$ cubic B-spline basis $\{b_i(x)\}_{i=1}^r$ over Ω . Then, we augment the cubic B-spline basis with its damped versions and get

$$\mathbb{B}_k = \{b_i(x)\}_{i=1}^r \cup \{b_i(x) \cos(\alpha x)\}_{i=1}^r \cup \{b_i(x) \sin(\alpha x)\}_{i=1}^r, \quad (15)$$

where $k = 3r$. Because the sB-spline basis is directly obtained by damping B-spline it inherits the compact support of the B-spline basis (de Boor, 2000). Therefore each of \mathbf{G} , \mathbf{C} and \mathbf{M} is still a banded sparse matrix, and so will be the precision matrix Σ_w^{-1} and the design matrix Φ .

While preserving the original computational efficiency from cubic B-spline basis, the sB-spline approximation has significantly better approximation accuracy, particular when k is small and α is large. This can be seen from Fig. 2; When $\alpha = 2\pi$, the sB-spline approximation reduces the correlation error to less than 0.2 with $k = 20$, but the original cubic B-spline requires k more than 80 to achieve the same accuracy. The

sB-spline approximation also inherits the convergence result in Theorem 2, as summarized in the corollary below:

Corollary 1 (Convergence of sB-spline Approximation). *Let $\Omega = [a, b]$ where $a, b \in \mathbb{R}^+$ and let $g \sim \text{sGP}$ with parameters $\alpha, \sigma > 0$. Assume \mathbb{B}_k is a set of k sB-splines constructed with equally spaced knots over Ω as defined in Eq. (15), and \tilde{g}_k denotes the corresponding FEM approximation defined as in Eq. (9), then:*

$$\lim_{k \rightarrow \infty} \mathcal{C}_k(x_1, x_2) = \mathcal{C}(x_1, x_2),$$

for any $x_1, x_2 \in \Omega$, where $\mathcal{C}(x_1, x_2) = \text{Cov}[g(x_1), g(x_2)]$, $\mathcal{C}_k(x_1, x_2) = \text{Cov}[\tilde{g}_k(x_1), \tilde{g}_k(x_2)]$.

Proof. This corollary directly follows from Theorem 2 with the observation that Eq. (15) contains the original cubic B-spline basis. □

4. Prior for the sGP

To perform Bayesian inference with $g \sim \text{sGP}(\alpha, \sigma)$, it is crucial to define a prior on the standard deviation (SD) parameter σ in an interpretable manner. However, the effect and interpretation of σ on the fitted function vary significantly with the choice of α , even though it can always be viewed as the deviation size from the corresponding sinusoidal space $\text{Null}\{L\}$. Therefore, instead of assigning prior on the original SD σ , we propose to assign the prior on the predictive standard deviation (PSD) (Zhang et al., 2023b), which is a one-to-one transformation of σ with a consistent interpretation across different values of α .

Given a once-differentiable function g and a prediction unit $h > 0$, the PSD is defined as:

$$\text{SD} \left[g(x+h) \middle| g(x), g^{(1)}(x) \right], \tag{16}$$

which quantifies the uncertainty in predicting the function g at h units ahead, using the current value and the value of its derivative. In practice, the unit h can be chosen based on the practical requirements of the application. For the sGP, the PSD has a simple formula, as given in the following corollary:

Corollary 2 (Predictive Standard Deviation of the sGP). *Let $g \sim \text{sGP}$ with parameters $\alpha, \sigma > 0$, then:*

$$\sigma(h) = SD\left[g(x+h) \middle| g(x), g^{(1)}(x)\right] = \frac{\sigma}{\alpha} \sqrt{\left(\frac{h}{2} - \frac{\sin(2\alpha h)}{4\alpha}\right)}, \quad (17)$$

for any $x, h \in \mathbb{R}^+$.

Proof. This corollary is a direct consequence of the state-space representation in Theorem 1. \square

It is worth noting that the PSD $\sigma(h)$ of the sGP does not depend on the current location x , as shown in Eq. (17). This feature distinguishes our approach from that of Sorbye and Rue (2014), which uses the marginal standard deviation $SD[g(x)]$ and hence requires a set of reference locations to be specified. Additionally, the PSD in our approach is computed using the true sGP and is therefore invariant to the approximation choices, such as the number and placement of the knots. Finally, we choose an exponential prior for $\sigma(h)$ that encourages g to behave like a sinusoidal function, which is motivated by Simpson et al. (2017). The prior for the original σ is then recovered by scaling the exponential prior for $\sigma(h)$ with $\alpha/\sqrt{(h/2 - \sin(2\alpha h)/4\alpha)}$.

5. Examples

5.1. Canadian Mortality

In this example, we utilize the sGP to analyze the cause-specific mortality counts in Ontario from Statistics Canada. These data were collected weekly from Jan 9th 2010 to January 1st 2022. To illustrate the methodology, we consider the mortality counts due to heart attack, influenza and accidental injuries. We fit models using data prior to March 1st, 2020 and use the remaining data to quantify the excess mortality of each cause during the COVID-19 pandemic.

For all three datasets (heart attack, influenza, and accidental injuries), we use the following model:

$$\begin{aligned} y_i | \lambda_i &\sim \text{Poisson}(\lambda_i), \\ \log(\lambda_i) &= \eta_i = \beta_0 + \beta_1 x_i + g(x_i) + \xi_i, \\ g &\sim \text{sGP}(a = 2\pi, \sigma), \quad \xi_i \sim N(0, \sigma_\xi^2), \end{aligned} \quad (18)$$

where y_i denotes the mortality count and x_i denotes the time of measurement in years since Jan 9th 2010. The observation-level random effect ξ_i is used to capture the overdispersion. We assign independent normal priors with mean 0 and variance 1000 to the fixed effects (β_0 and β_1) and the boundary conditions of the sGP. For the variance parameters σ and σ_ξ , we use exponential priors such that:

$$\mathbb{P}(\sigma(1) > 0.01) = 0.5, \quad \mathbb{P}(\sigma_\xi > 1) = 0.5, \quad (19)$$

where $\sigma(1)$ is the 1-year PSD of the sGP g defined in Section 4.

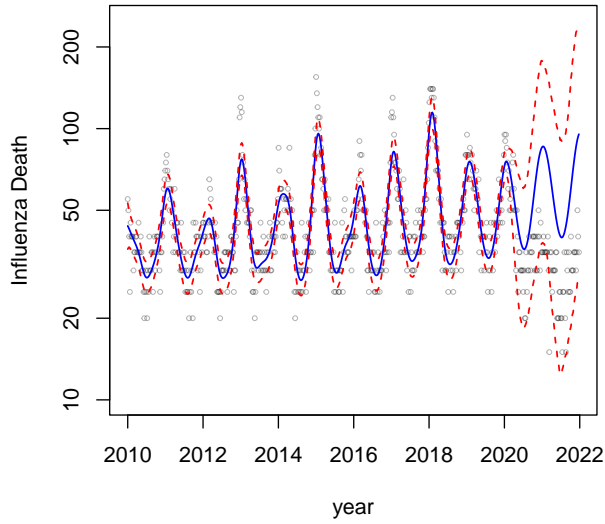
To perform inference on the 1-year sGP, we use the augmented space method described in Section 2.1. The results of the analysis for the three mortality rates are presented in Fig. 3. The mortality due to influenza shows a much larger deviation from yearly periodicity compared to heart attack mortality. In particular, the peak mortality rate in 2015 is much higher than peaks in the preceding years. Consequently, the prediction uncertainty of g is greater for influenza compared to for heart attack. On the other hand, the effect of seasonality in injury data is relatively small compared to that in influenza and heart attack data. The inference results for total excess mortality during the COVID-19 period are presented in Fig. 4. The posteriors indicate strong evidence of negative excess mortality in influenza and likely positive excess mortality in accidental injury. However, for heart attack, there is no evidence of excess mortality in either direction.

5.2. Lynx Counts

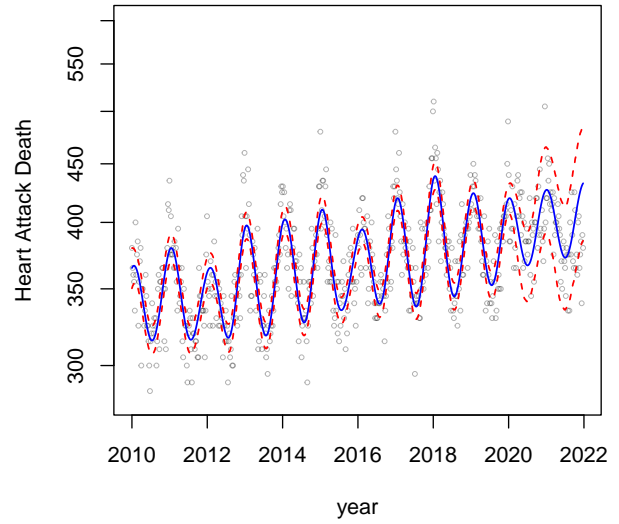
In this section, we analyze the annual counts of trapped lynxes in Canada for 1821–1934 (Campbell and Walker, 1977), with the following model:

$$\begin{aligned} y_i | \lambda_i &\sim \text{Poisson}(\lambda_i), \quad \log(\lambda_i) = \eta_i = \beta_0 + g_c(x_i) + g_{c/2}(x_i) + \xi_i, \\ g_j &\sim \text{sGP}\left(a = \frac{2\pi}{j}, \sigma_j\right) \text{ for } j \in \left\{c, \frac{c}{2}\right\}, \quad \xi_i \sim N(0, \sigma_\xi^2), \end{aligned} \quad (20)$$

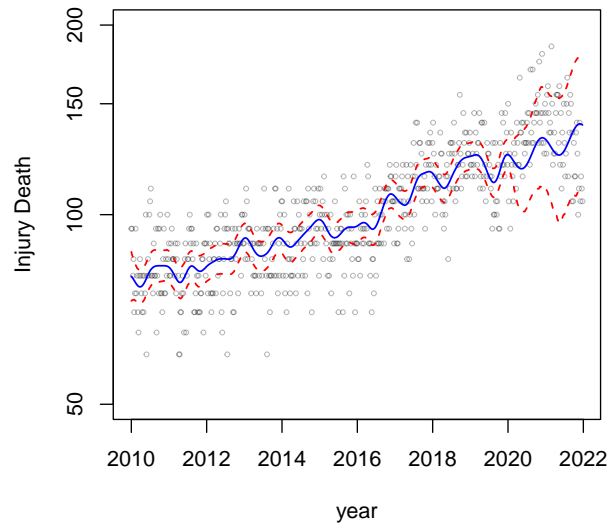
where y_i denotes the counts of trapped lynxes in Canada and x_i denotes the year since 1821. We assume the variation in lynxes counts is driven by two independent sGPs, with c years ($\alpha = 2\pi/c$) and $c/2$ years cycle ($\alpha = 4\pi/c$). We assign independent exponential priors such that $\mathbb{P}(\sigma_j(50) > 1) = 0.01$ for each



(a)

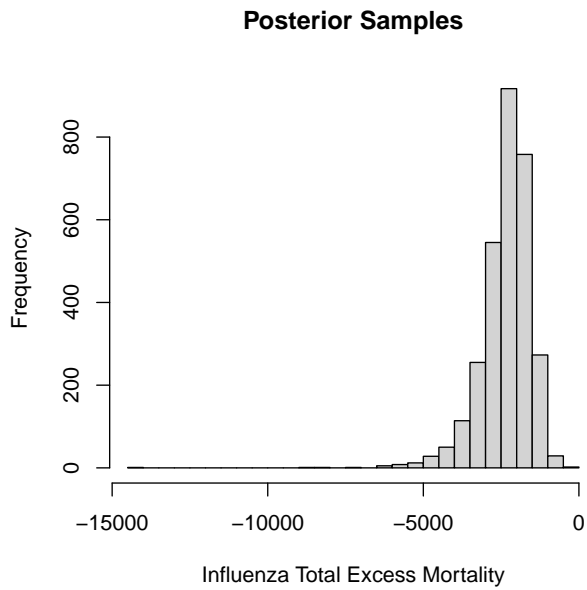


(b)

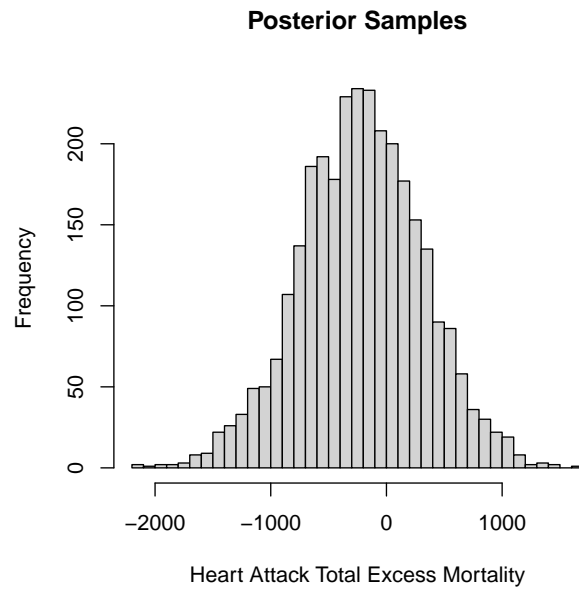


(c)

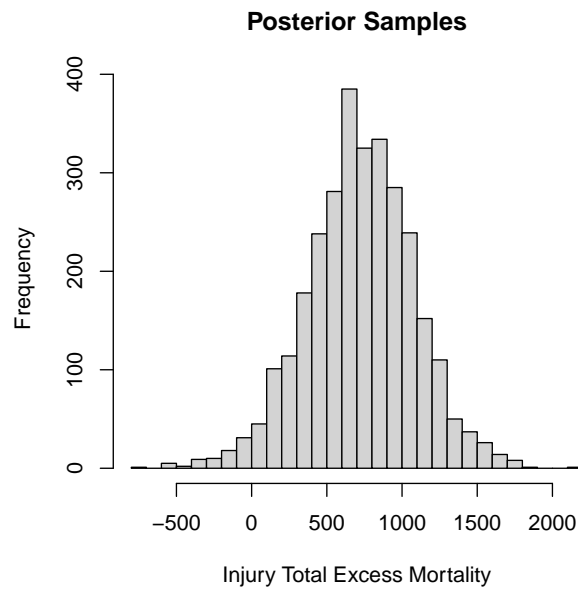
Figure 3: Inferential Results for the mortality rates over time in Section 5.1. Figures (a)-(c) display the posterior distributions of $\exp[\beta_0 + \beta_1 x_i + g(x_i)]$ and the death counts (points). The posterior means are shown in the blue solid lines and the 95 percent posterior intervals are shown in the red dashed lines.



(a)



(b)



(c)

Figure 4: Inferential Results for total excess mortality in Section 5.1. Figures (a)-(c) show the posterior samples of the total excess mortality, where each sample is the sum of the difference between a posterior sample of the predicted death and the actual death counts.

$j \in \{c, c/2\}$, and $\mathbb{P}(\sigma_\xi > 1) = 0.01$. All the boundary conditions in the sGPs and the intercept β_0 are assigned with independent normal prior $N(0, 1000)$. The year of periodicity c is assumed unknown between 6 years to 12 years, and we place a discrete uniform prior for c from 6 to 12 years with 0.1 year spacing.

We carry out the inference of the sGPs with the state-space approach described in Section 2.1. The inferential results are summarized in Fig. 5. Based on Fig. 5(a), it is most likely that the data exhibits a roughly 10.1 years cyclic variation, which is close to the duration of the solar cycle. The two sGPs well capture the quasi-periodic behaviors in the variation, as illustrated in Fig. 5(b).

5.3. Sunspot Data

In this example, we analyze the yearly mean sunspot data from the World Data Center SILSO, Royal Observatory of Belgium, Brussels (SILSO World Data Center, 2022), with the following model:

$$\begin{aligned} y_i &= g_s(x_i) + g_{tr}(x_i) + \epsilon_i, \\ g_s &\sim \text{sGP}\left(a = \frac{2\pi}{c}, \sigma_s\right), \quad g_{tr} \sim \text{IWP}_3(\sigma_{tr}), \\ \epsilon_i &\sim N(0, \sigma_\epsilon^2), \end{aligned} \tag{21}$$

where y_i denotes the log-transformed yearly mean sunspot, and x_i denotes the year of measurement since 1700.

We model the seasonal variation in yearly mean sunspots with an sGP model with periodicity around c years, denoted as g_s . The long-term trend g_{tr} is modelled with a third-order Integrated Wiener process (IWP-3) with smoothing parameter σ_{tr} . For variance parameters, we use independent exponential priors such that $\mathbb{P}(\sigma_c(50) > 1) = 0.5$, $\mathbb{P}(\sigma_{tr}(50) > 5) = 0.5$ and $\mathbb{P}(\sigma_\epsilon > 1) = 0.1$. All the boundary conditions in the sGP are assigned with independent normal prior $N(0, 1000)$. The year of periodicity c is assumed unknown between 8 years to 13 years, and we place a discrete uniform prior for c from 8 to 13 years with 0.1 year spacing.

To facilitate the computation, we then approximate g_{tr} using 100 O-spline basis functions introduced in (Zhang et al., 2023b), and g_s using 300 sB-spline basis functions as described in Section 3.1. All the basis functions are constructed with equally spaced knots. The inferential results are summarized in Fig. 6. Similar to the results in Section 5.2, the posterior distribution of c is concentrated between 9.5 years to

11.5 years, close to the duration of the solar cycle.

5.4. CO2 Variation

In this section, we will study the atmospheric Carbon Dioxide (CO2) concentrations data collected from an observatory in Hawaii from 1960 to 2021. The observations were collected monthly before May 1974 and weekly afterward.

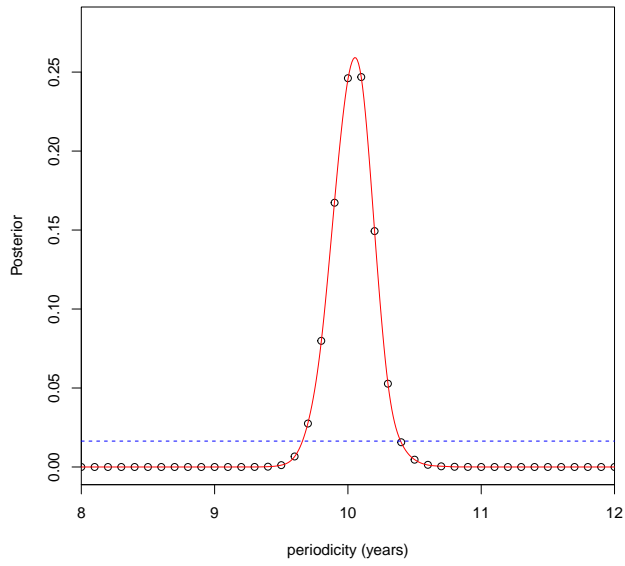
Previous analyses have suggested the presence of several periodic components in addition to the obvious yearly cycle in the CO2 variation. Rust et al. (1979) analyzed the data from this observatory and hypothesized that besides the obvious yearly cyclic variation, two longer periodic components also likely exist, due to the southern oscillation index (ENSO) and solar activity cycles. Therefore, Rust et al. (1979) adopted a model with an exponential function for the trend, one sinusoidal function and its first harmonic component for the annual cycle, and two additional sinusoidal functions for the ENSO and solar cycles. In a later study of the climate oscillation, Scafetta (2010) also identified a 10.4-year cycle induced by the solar cycle, and an additional 9.1-year cycle induced by long lunar tidal behaviors

Subsequently, both Rasmussen (2003) and Solin and Särkkä (2014) analyzed the CO2 data with Gaussian process regressions. They assumed the CO2 concentration consists of an increasing long-term trend, a pronounced yearly seasonal variation, and some irregular noise. Rasmussen (2003) suggested that the seasonal variation in the CO2 variation is smooth but not exactly periodic, and both Rasmussen (2003) and Solin and Särkkä (2014) chose to model the quasi-periodic seasonal variation as one GP with covariance being the product of the canonical periodic covariance and the Matern covariance with $\nu = 3/2$ or ∞ .

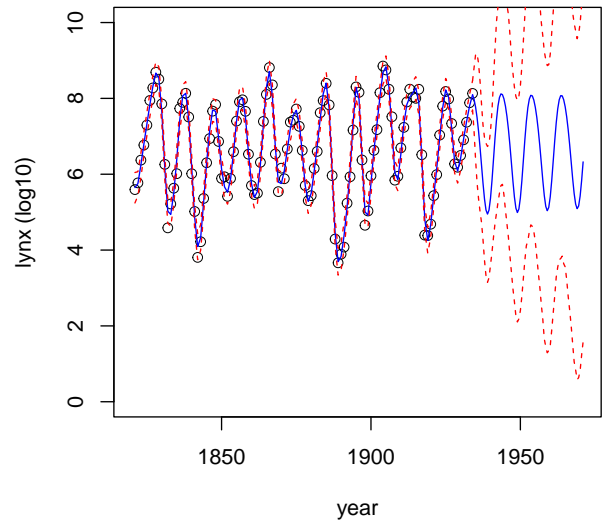
Based on these existing studies, we consider the following model (M1):

$$\begin{aligned}
 y_i &= g_{tr}(x_i) + g_1(x_i) + g_{\frac{1}{2}}(x_i) + g_{\frac{44}{12}}(x_i) + g_{9.1}(x_i) + g_{10.4}(x_i) + e_i, \\
 g_s &\sim \text{sGP}\left(a = \frac{2\pi}{s}, \sigma_s\right), \text{ for } s \in \left\{1, \frac{1}{2}, \frac{44}{12}, 9.1, 10.4\right\} \\
 g_{tr} &\sim \text{IWP-3}(\sigma_{tr}), \quad e_i \sim N(0, \sigma_e^2),
 \end{aligned} \tag{22}$$

where each y_i denotes the CO2 concentration and x_i denotes the time of measurement since March 30, 1960, in years. The long-term trend g_{tr} is modelled using a third-order IWP with smoothing parameter σ_{tr} . The seasonal variation is modelled as the sum of five separate sGPs: the first two sGPs capture

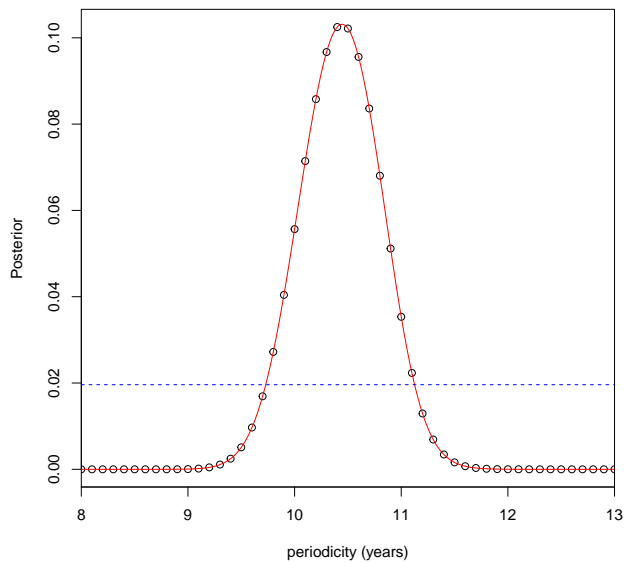


(a)

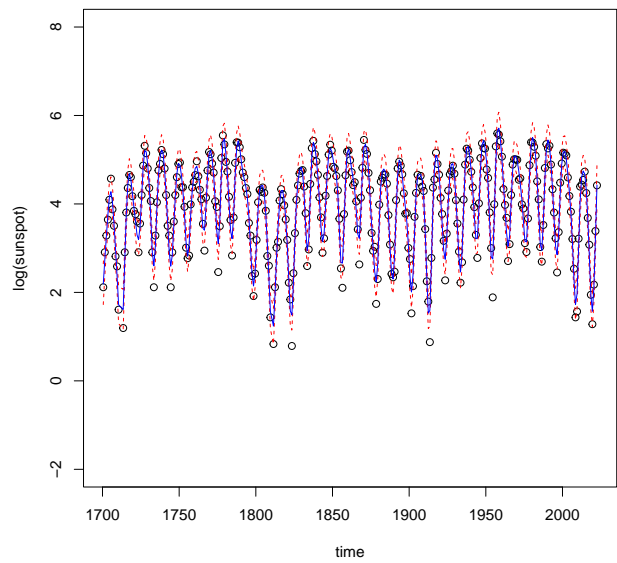


(b)

Figure 5: Inferential Results for the Lynx analysis in Section 5.2. Figure (a) shows the posterior distribution of the unknown periodicity year c . Figure (b) shows the posterior distribution of $g_c + g_{c/2}$: posterior mean shown in the blue line, 95 credible intervals shown in the red lines, and observations shown in circles.



(a)



(b)

Figure 6: Inferential Results for the sunspot analysis in Section 5.3. Figure (a) shows the posterior distribution of the unknown periodicity year c . Figure (b) shows the posterior distribution of $g_s + g_{tr}$: posterior mean shown in the blue line, 95 credible intervals shown in the red lines, and observations shown in circles.

the one-year cycle and its first-order harmonic, and the third sGP capture the 44-month ENSO cycles suggested in Rust et al. (1979), and the fourth and fifth sGPs respectively capture the 9.1-year lunar cycle and 10.4-year solar cycle suggested in Scafetta (2010). All the components in the model are considered to be independent.

In contrast to Rasmussen (2003) and Solin and Särkkä (2014) where all the hyperparameters are estimated through maximizing marginal likelihood, we assign independent exponential priors to all the variance parameters such that:

$$\begin{aligned} \mathbb{P}(\sigma_s(10) > 1) &= 0.5, \text{ for } s \in \left\{ 1, \frac{1}{2}, \frac{44}{12}, 9.1, 10.4 \right\} \\ \mathbb{P}(\sigma_{tr}(10) > 30) &= 0.5, \quad \mathbb{P}(\sigma_e > 1) = 0.5. \end{aligned} \tag{23}$$

All the boundary conditions in the sGP or IWP are assigned with independent priors $N(0, 1000)$. As a comparison, we also consider an exact periodic model (M2):

$$\begin{aligned} y_i &= g_{tr}(x_i) + g_1(x_i) + g_{\frac{1}{2}}(x_i) + g_{\frac{44}{12}}(x_i) + g_{9.1}(x_i) + g_{10.4}(x_i) + e_i, \\ g_s(x) &= v_{s_1} \cos\left(\frac{2\pi x}{s}\right) + v_{s_2} \sin\left(\frac{2\pi x}{s}\right), \text{ for } s \in \left\{ 1, \frac{1}{2}, \frac{44}{12}, 9.1, 10.4 \right\} \\ g_{tr} &\sim \text{IWP-3}(\sigma_{tr}), \quad e_i \sim N(0, \sigma_e^2), \end{aligned} \tag{24}$$

where all the sGP components in M1 are replaced with just their corresponding sinusoidal functions, and all the priors are the same as in M1.

In order to improve computational efficiency, we adopt FEM approximations for all the \mathcal{GP} s in M1 and M2, with basis functions constructed using equally spaced knots. Specifically, we utilize the sB-splines approximation with 90 basis functions for the sGP models, and the O-Spline approximation (Zhang et al., 2023b) with 50 basis functions for the IWP model. Once the models M1 and M2 are fitted, we use them to forecast CO2 variation up to the year 2030. The inference and prediction results are summarized in Fig. 7, Fig. 8 and Table 1.

As shown in Fig. 7, the sGP-based model (M1) produces a much more stable prediction than the exact-periodic model (M2), demonstrated by the width of the posterior interval in the forecast. This is because, the value of $\sigma_{tr}(10)$ in M2 is estimated to be much larger (Post Median: 100.6) compared to in

	1st Quantile	Median	3rd Quantile
$\sigma_{tr}(10)$	0.4371 (102.05)	0.6446 (120.81)	0.9462 (139.49)
$\sigma_1(10)$	1.8179 (-)	2.4542 (-)	3.1709 (-)
$\sigma_{\frac{1}{2}}(10)$	1.8179 (-)	2.4542 (-)	3.1709 (-)
$\sigma_{\frac{44}{12}}(10)$	0.4004 (-)	0.4514 (-)	0.5019 (-)
$\sigma_{9.1}(10)$	0.004248 (-)	0.01045 (-)	0.02445 (-)
$\sigma_{10.4}(10)$	0.01090 (-)	0.02035 (-)	0.03335 (-)
σ_ϵ	0.5870 (0.6099)	0.5928 (0.6159)	0.5988 (0.6220)

Table 1: Posterior summary of variance parameters for the CO2 example in Section 5.4. Results from M2 are shown in parenthesis.

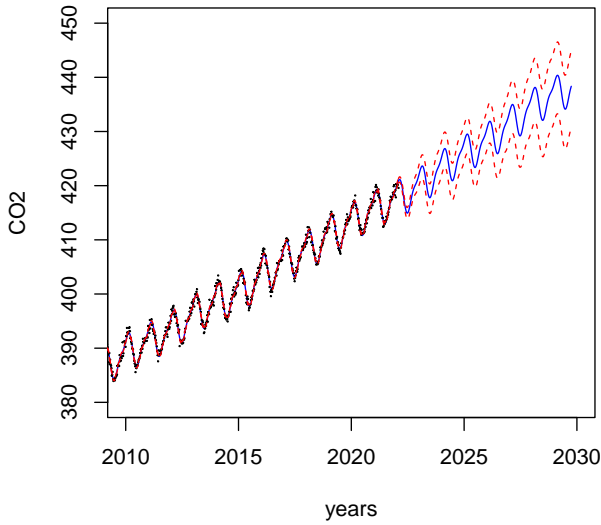
M1 (Post Median: 0.593), due to the failure of M1 to accommodate the quasi-periodic behavior of the seasonal variation. This difference can be further confirmed in Fig. 8, where the derivative of the long-term trend has smooth sample paths in M1 but very wiggly sample paths in M2.

6. Discussion

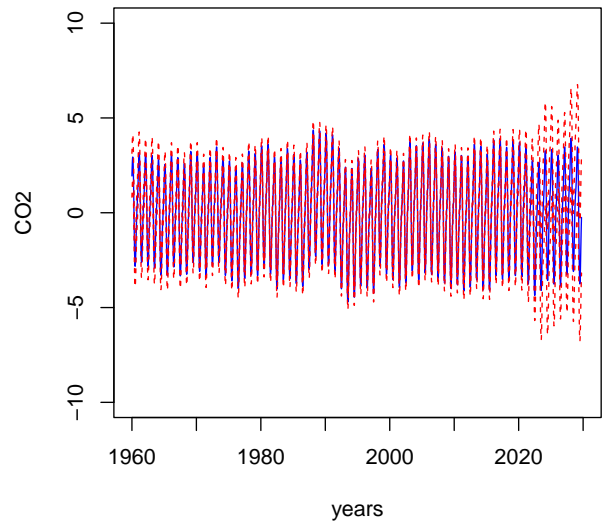
In this paper, we introduced a class of Gaussian processes called seasonal Gaussian processes (sGP) for making model-based inference on quasi-periodic functions. We then proposed an accurate and computationally efficient sB-spline approximation to the sGP, which can handle densely irregularly spaced locations. The proposed approximation is shown to converge to the sGP as the number of basis functions increases, both theoretically and numerically. We implemented our proposed approaches in a flexible and scalable manner using modern approximate Bayesian inference algorithms, as described in Stringer (2020), and demonstrated their practical usage in diverse real data applications.

While our focus was on making fully Bayesian inference for the unknown quasi-periodic function g , our proposed approaches could also be implemented in a mixed effect model with parameters estimated through maximum likelihood (Rasmussen, 2003) or generalized cross-validation (Golub et al., 1979). An interesting avenue for future work is to extend our approach to incorporate adaptive modeling of the sGP, where the standard deviation parameter σ varies over time. This could be achieved using a strategy similar to the one described in Yue et al. (2014).

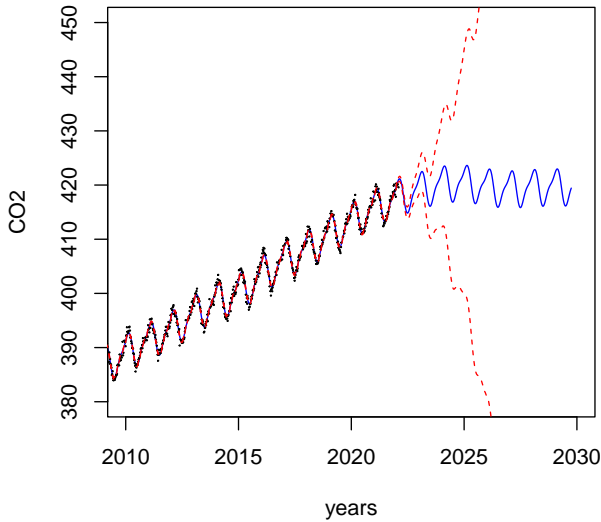
We have made the software that implements our proposed methods available on a Github repository, which can be found at <https://github.com/AgueroZZ/sGPfit>.



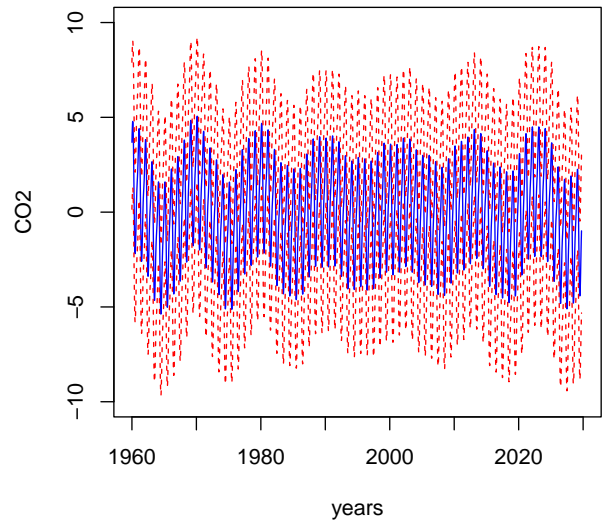
(a) M1: Overall mean CO2 concentration



(b) M1: Seasonal variation

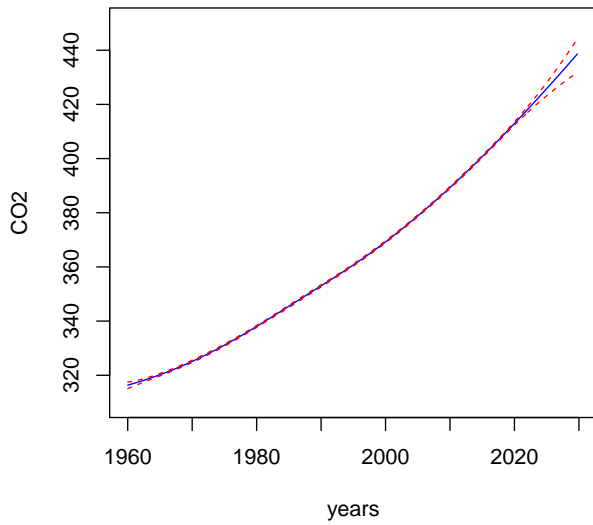


(c) M2: Overall mean CO2 concentration

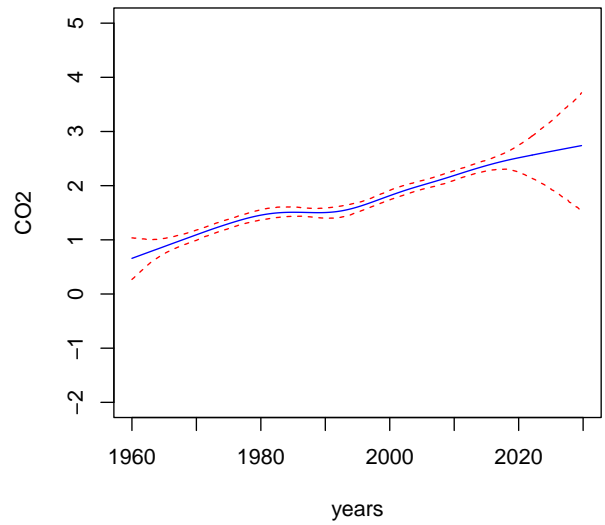


(d) M2: Seasonal variation

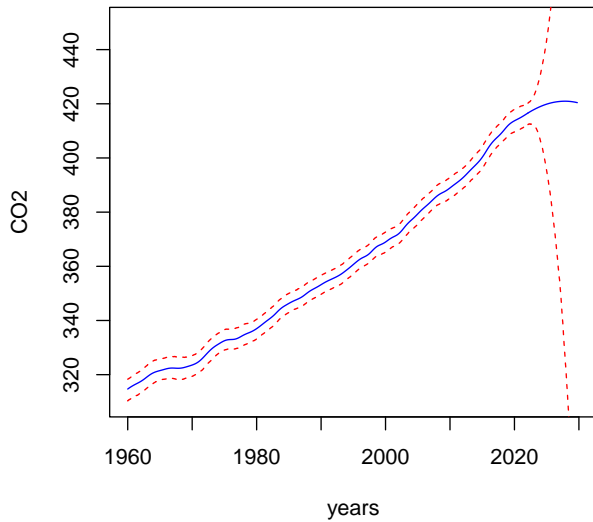
Figure 7: Inferential Results for the CO2 example in Section 5.4. (a,c) display the posterior of the overall mean CO2 concentration over years (i.e. $g_{tr} + \sum_s g_s$). (b,d) show the posterior of the overall seasonal component in the CO2 concentration (i.e. $\sum_s g_s$). In (a)-(d), the blue solid lines denote the posterior mean, and the red dashed lines denote the 95 percent posterior credible interval. The prediction result from M1 is more stable than that from M2, as shown by the width of the interval.



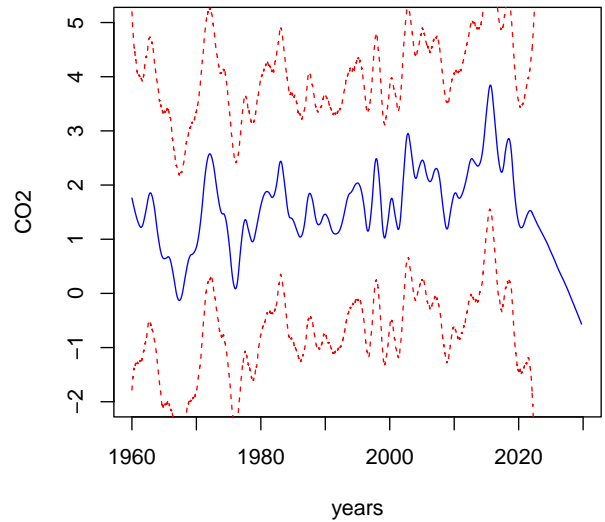
(a) M1: Long-term trend g_{tr}



(b) M1: Inference of g'_{tr}



(c) M2: Long-term trend g_{tr}



(d) M2: Inference of g'_{tr}

Figure 8: Detailed inferential results for the CO2 example in Section 5.4. (a,c) display the posterior distribution of the long-term trend; (b,d) display the posterior distribution of the first derivative of the long-term trend. In (a)-(d), the blue solid lines denote the posterior mean, and the red dashed lines denote the 95 percent posterior credible interval. The derivative of g_{tr} is estimated to be much smoother in M1, whereas in M2 the result is oscillating due to the unaccounted quasi-periodicity.

R-package: The R-package *sGPfit* that implements the proposed methodology in the paper can be found at github.com/AgueroZZ/sGPfit.

Codes and Data: All the data used in this paper are publicly available for download. The mortality data in Section 5.1 is available at statcan.gc.ca. The lynx data in Section 5.2 is available in the R package *datasets* (version 4.2.1). The sunspot data in Section 5.3 is available at sidc.be/silso. The CO2 data in Section 5.4 can be accessed from scrippsco2.ucsd.edu.

The codes to replicate each of the examples can be found at github.com/AgueroZZ/sGPcode.

Supplement: The online supplement includes an R-markdown tutorial that provides step-by-step guidance for users to implement our proposed approach using the Lynx dataset in R.

References

- Ansley, C. F. and Kohn, R. (1990). Filtering and smoothing in state space models with partially diffuse initial conditions. *Journal of Time Series Analysis*, 11(4):275–293.
- Ansley, C. F., Kohn, R., and Wong, C.-M. (1993). Nonparametric spline regression with prior information. *Biometrika*, 80(1):75–88.
- Bilodeau, B., Stringer, A., and Tang, Y. (2022). Stochastic convergence rates and applications of adaptive quadrature in bayesian inference. *Journal of the American Statistical Association*, pages 1–11.
- Brenner, S. C., Scott, L. R., and Scott, L. R. (2008). *The mathematical theory of finite element methods*, volume 3. Springer.
- Campbell, M. and Walker, A. (1977). A survey of statistical work on the mackenzie river series of annual canadian lynx trappings for the years 1821-1934 and a new analysis. *Journal of the Royal Statistical Society: Series A (General)*, 140(4):411–431.
- de Boor, C. (2000). *A practical guide to splines*. Springer.

- Golub, G. H., Heath, M., and Wahba, G. (1979). Generalized cross-validation as a method for choosing a good ridge parameter. *Technometrics*, 21(2):215–223.
- Harvey, A. C. et al. (1990). Forecasting, structural time series models and the kalman filter. *Cambridge Books*.
- Lindgren, F. and Rue, H. (2008). On the second-order random walk model for irregular locations. *Scandinavian Journal of Statistics*, 35(4):691 – 700.
- Lindgren, F., Rue, H., and Lindstrom, J. (2011). An explicit link between gaussian fields and gaussian markov random fields: the stochastic partial differential equation approach. *Journal of the Royal Statistical Society, Series B (Statistical Methodology)*, 73(4):423–498.
- Rasmussen, C. E. (2003). Gaussian processes in machine learning. In *Summer school on machine learning*, pages 63–71. Springer.
- Roberts, S., Osborne, M., Ebden, M., Reece, S., Gibson, N., and Aigrain, S. (2013). Gaussian processes for time-series modelling. *Philosophical Transactions of the Royal Society A: Mathematical, Physical and Engineering Sciences*, 371(1984):20110550.
- Rue, H. and Held, L. (2005). *Gaussian Markov Random Fields: Theory and Applications*. Chapman and Hall/CRC Press.
- Rue, H., Martino, S., and Chopin, N. (2009). Approximate bayesian inference for latent gaussian models by using integrated nested laplace approximations. *Journal of the Royal Statistical Society. Series B (Statistical Methodology)*, 71(2):319 – 392.
- Rust, B. W., Rotty, R. M., and Marland, G. (1979). Inferences drawn from atmospheric co2 data. *Journal of Geophysical Research: Oceans*, 84(C6):3115–3122.
- Särkkä, S. and Solin, A. (2019). *Applied stochastic differential equations*, volume 10. Cambridge University Press.
- Scafetta, N. (2010). Empirical evidence for a celestial origin of the climate oscillations and its implications. *Journal of Atmospheric and Solar-Terrestrial Physics*, 72(13):951–970.

- Schultz, M. H. (1969). Approximation theory of multivariate spline functions in sobolev spaces. *SIAM Journal on Numerical Analysis*, 6(4):570–582.
- SILSO World Data Center (1700-2022). The International Sunspot Number. *International Sunspot Number Monthly Bulletin and online catalogue*.
- Simpson, D., Rue, H., Martins, T. G., Riebler, A., and Sorbye, S. H. (2017). Penalising model component complexity: A principled, practical approach to constructing priors. *Statistical Science*, 32(1):1 – 28.
- Solin, A. and Särkkä, S. (2014). Explicit link between periodic covariance functions and state space models. In *Artificial Intelligence and Statistics*, pages 904–912. PMLR.
- Sorbye, S. H. and Rue, H. (2014). Scaling intrinsic gaussian markov random field priors in spatial modelling. *Spatial Statistics*, 8:39–51.
- Stringer, A. (2020). Implementing approximate bayesian inference using adaptive quadrature: the aghq package. *arXiv:2101.04468 [stat.CO]*.
- Stringer, A., Brown, P., and Stafford, J. (2022). Fast, scalable approximations to posterior distributions in extended latent gaussian models. *Journal of Computational and Graphical Statistics*, pages 1–36.
- Yue, Y. R., Simpson, D., Lindgren, F., and Rue, H. (2014). Bayesian adaptive smoothing splines using stochastic differential equations.
- Zhang, Z., Stringer, A., Brown, P., and Stafford, J. (2023a). Bayesian inference for cox proportional hazard models with partial likelihoods, nonlinear covariate effects and correlated observations. *Statistical Methods in Medical Research*, 32(1):165–180.
- Zhang, Z., Stringer, A., Brown, P., and Stafford, J. (2023b). Model-based smoothing with integrated wiener processes and overlapping splines. *arXiv preprint arXiv:2302.02053*.

Appendix A: Derivation of the sGP covariance

Proposition 1 (Covariance Function of the Seasonal Gaussian Process). *Let $g \sim sGP(\alpha, \sigma)$. Then g has a covariance function:*

$$\begin{aligned} C(x_1, x_2) &= \left(\frac{\sigma}{\alpha}\right)^2 \left[\frac{x_1}{2} \cos(\alpha(x_2 - x_1)) - \frac{\cos(\alpha x_2) \sin(\alpha x_1)}{2\alpha} \right] \\ &= \left(\frac{\sigma}{\alpha}\right)^2 \left[\frac{\cos(\alpha x_2) x_1}{2} \cos(\alpha x_1) + \left(\frac{\sin(\alpha x_2) x_1}{2} - \frac{\cos(\alpha x_2)}{2\alpha} \right) \sin(\alpha x_1) \right], \end{aligned} \quad (25)$$

for any $x_1, x_2 \in \mathbb{R}^+$ such that $x_1 \leq x_2$.

Proof. It is obvious that the differential operator L is linear. Define $\mathbf{g}_{aug}(x) = (g(x), g'(x))^T$ and therefore $\mathbf{g}'_{aug}(x) = (g'(x), g''(x))^T$, then the SDE can be rewritten in the vector form:

$$\mathbf{g}'_{aug} = \mathbf{F} \mathbf{g}_{aug} + \mathbf{L}W, \quad (26)$$

where $\mathbf{F} = \begin{bmatrix} 0 & 1 \\ -\alpha^2 & 0 \end{bmatrix}$ and $\mathbf{L} = \begin{bmatrix} 0 \\ \sigma \end{bmatrix}$.

Using the result from Särkkä and Solin (2019) (section 4.3), the solution of the linear SDE can be written as:

$$\begin{aligned} \mathbf{g}_{aug}(x) &= \exp(\mathbf{F}x) \mathbf{g}_{aug}(0) + \int_0^x \exp(\mathbf{F}(x - \tau)) \mathbf{L}W(\tau) d\tau \\ &= \int_0^x \exp(\mathbf{F}(x - \tau)) \mathbf{L}W(\tau) d\tau, \end{aligned} \quad (27)$$

where $\exp(\mathbf{F}x)$ denotes the matrix exponential defined as $\exp(\mathbf{F}x) = \sum_k \frac{\mathbf{F}^k x^k}{k!}$.

Note that $\mathbf{F}^{2k} = (-\alpha^2)^k \mathbf{I}$ and $\mathbf{F}^{2k+1} = (-\alpha^2)^k \mathbf{F}$. With Taylor series, the first component of $\mathbf{g}_{aug}(x)$ can be therefore written as:

$$g(x) = \int_0^x \frac{\sigma}{\alpha} \sin(\alpha(x - \tau)) W(\tau) d\tau. \quad (28)$$

Assume arbitrary $0 < x_1 \leq x_2$, the covariance function can be computed for g as:

$$\begin{aligned} k(x_1, x_2) &= \int_0^{x_1} \frac{\sigma}{\alpha} \sin(\alpha(x_1 - \tau)) \frac{\sigma}{\alpha} \sin(\alpha(x_2 - \tau)) d\tau \\ &= \left(\frac{\sigma}{\alpha}\right)^2 \left[\frac{x_1}{2} \cos(\alpha(x_2 - x_1)) - \frac{\cos(\alpha x_2) \sin(\alpha x_1)}{2\alpha} \right], \end{aligned} \quad (29)$$

using properties of Gaussian white noise (Harvey et al., 1990).

□

Appendix B: Proof of the State-Space Representation

Theorem 1 (State Space Representation of the sGP). *Consider $g \sim sGP(\alpha, \sigma)$, and let $\mathbf{s} = \{s_1, \dots, s_n\} \subset \mathbb{R}^+$ denotes a set of n sorted locations and spacing $d_1 = s_1$ and $d_i = s_i - s_{i-1}$ for $i \in \{2, \dots, n\}$. Then the augmented vector $\mathbf{g}_{aug}(s_i) = [g(s_i), g'(s_i)]^T$ can be written as a Markov model:*

$$\mathbf{g}_{aug}(s_{i+1}) = \mathbf{R}_{i+1} \mathbf{g}_{aug}(s_i) + \boldsymbol{\epsilon}_{i+1}, \quad (30)$$

where $\boldsymbol{\epsilon}_i \stackrel{ind}{\sim} N(0, \boldsymbol{\Sigma}_i)$. The 2×2 matrices \mathbf{R}_i and $\boldsymbol{\Sigma}_i = \mathbf{Q}_i^{-1}$ are respectively defined as:

$$\mathbf{R}_i = \begin{bmatrix} \cos(\alpha d_i) & \frac{1}{\alpha} \sin(\alpha d_i) \\ -\alpha \sin(\alpha d_i) & \cos(\alpha d_i) \end{bmatrix}, \quad \boldsymbol{\Sigma}_i = \sigma^2 \begin{bmatrix} \frac{1}{\alpha^2} \left(\frac{d_i}{2} - \frac{\sin(2\alpha d_i)}{4\alpha} \right) & \frac{\sin^2(\alpha d_i)}{2\alpha^2} \\ \frac{\sin^2(\alpha d_i)}{2\alpha^2} & \frac{2\alpha d_i + \sin(2\alpha d_i)}{4\alpha} \end{bmatrix}. \quad (31)$$

Proof. To show the above Markov representation, note that the value of $g(s_{i+1})$ given $g(s_i)$ can be written similarly as (Särkkä and Solin, 2019):

$$\mathbf{g}_{aug}(s_{i+1}) = \exp(\mathbf{F} d_{i+1}) \mathbf{g}_{aug}(s_i) + \int_{s_i}^{s_{i+1}} \exp(\mathbf{F}(s_{i+1} - \tau)) \mathbf{L} W(\tau) d\tau.$$

Recall that $\mathbf{F}^{2k} = (-a^2)^k \mathbf{I}$ and $\mathbf{F}^{2k+1} = (-a^2)^k \mathbf{F}$, then apply the Taylor series expansion for both

components in the integral above. It then can be rewritten as:

$$\begin{aligned}
\mathbf{g}_{aug}(s_{i+1}) &= \exp(\mathbf{F}d_{i+1})\mathbf{g}_{aug}(s_i) + \int_{s_i}^{s_{i+1}} \exp(\mathbf{F}(s_{i+1} - \tau))\mathbf{L}W(\tau)d\tau \\
&= \mathbf{R}_{i+1}\mathbf{g}_{aug}(s_i) + \int_{s_i}^{s_{i+1}} \begin{bmatrix} \frac{1}{a} \sin(a(s_{i+1} - \tau)) \\ \cos(a(s_{i+1} - \tau)) \end{bmatrix} \sigma W(\tau)d\tau \\
&:= \mathbf{R}_{i+1}\mathbf{g}_{aug}(s_i) + \boldsymbol{\epsilon}_{i+1}.
\end{aligned} \tag{32}$$

Note that since each $\boldsymbol{\epsilon}_{i+1}$ involves integration at disjoint intervals, their independence follows from the property of Gaussian white noise (Harvey et al., 1990). To check its covariance matrix $\boldsymbol{\Sigma}_{i+1}$, note that:

$$\begin{aligned}
\boldsymbol{\Sigma}_{i+1} &= \sigma^2 \begin{bmatrix} \int_{s_i}^{s_{i+1}} \frac{1}{a^2} \sin^2(a(s_{i+1} - \tau))d\tau & \frac{1}{a} \int_{s_i}^{s_{i+1}} \sin(a(s_{i+1} - \tau)) \cos(a(s_{i+1} - \tau))d\tau \\ \frac{1}{a} \int_{s_i}^{s_{i+1}} \sin(a(s_{i+1} - \tau)) \cos(a(s_{i+1} - \tau))d\tau & \int_{s_i}^{s_{i+1}} \cos^2(a(s_{i+1} - \tau)) \end{bmatrix} \\
&= \sigma^2 \begin{bmatrix} \frac{1}{a^2} \left(\frac{d_{i+1}}{2} - \frac{\sin(2ad_{i+1})}{4a} \right) & \frac{\sin^2(ad_{i+1})}{2a^2} \\ \frac{\sin^2(ad_{i+1})}{2a^2} & \frac{2ad_{i+1} + \sin(2ad_{i+1})}{4a} \end{bmatrix},
\end{aligned} \tag{33}$$

which completes the proof. □

Appendix C: Finite Element Method

The Finite Element Method (FEM) used to construct the finite-dimensional approximation can be understood as the following procedures.

Given the (linear) stochastic differential equation (SDE) that defines the sGP model:

$$Lg(x) = \sigma\xi(x),$$

where $L = a^2 + \frac{d^2}{dx^2}$ is a linear differential operator and $\xi(x)$ is the standard Gaussian white noise process.

Let $\Omega \subset \mathbb{R}^+$ denotes a bounded interval of interest. Let $\mathbb{B}_k := \{\varphi_i, i \in [k]\}$ denote the set of k pre-specified basis functions, and let $\mathbb{T}_q := \{\phi_i, i \in [q]\}$ denote the set of q pre-specified test functions. We consider finite dimensional approximation with form $\tilde{g}(\cdot) = \sum_{i=1}^k w_i \varphi_i(\cdot)$. The weights $\mathbf{w} := [w_1, \dots, w_k]^T \in \mathbb{R}^k$ is a

set of random weights to be determined.

In our FEM construction, we used the sB-splines defined over Ω as the basis functions, and chose the test functions by $\mathbb{T}_k := \{\phi_i = L\varphi_i, i \in [k]\}$, which is called a least squares approximation in Lindgren et al. (2011). The distribution of the unknown weight vector can be found by fulfilling the weak formulation at the test function spaces \mathbb{T}_k , such that

$$\langle L\tilde{g}(x), \phi_i(x) \rangle \stackrel{d}{=} \sigma \langle \xi(x), \phi_i(x) \rangle, \quad (34)$$

for any test function $\phi_i \in \mathbb{T}_k$. This equation can also be vectorized as:

$$\langle L\tilde{g}(x), \phi_i(x) \rangle_{i=1}^k = H\mathbf{w},$$

where the ij component of the $k \times k$ H matrix can be computed as $H_{ij} = \langle L\varphi_j(x), L\varphi_i(x) \rangle_{i=1}^k$.

The inner product on the right $\langle \xi(x), \phi_i(x) \rangle_{i=1}^k$ will have Gaussian distribution with zero mean vector and covariance matrix H by properties of Gaussian white noise (Harvey et al., 1990). Therefore, the basis coefficients \mathbf{w} will be multivariate Gaussian with zero mean and covariance $H^{-1}HH^{-1} = H^{-1}$. Each element of the matrix H can be written as:

$$\begin{aligned} H_{ij} &= \langle L\varphi_j, L\varphi_i \rangle \\ &= \langle a^2\varphi_j + \frac{d^2\varphi_j}{dx^2}, a^2\varphi_i + \frac{d^2\varphi_i}{dx^2} \rangle \\ &= a^4\langle \varphi_j, \varphi_i \rangle + a^2\langle \frac{d^2\varphi_j}{dx^2}, \varphi_i \rangle + a^2\langle \varphi_j, \frac{d^2\varphi_i}{dx^2} \rangle + \langle \frac{d^2\varphi_j}{dx^2}, \frac{d^2\varphi_i}{dx^2} \rangle, \end{aligned} \quad (35)$$

hence $H = a^4G + C + a^2M$ with $G_{ij} = \langle \varphi_i, \varphi_j \rangle$, $C_{ij} = \langle \frac{d^2\varphi_i}{dx^2}, \frac{d^2\varphi_j}{dx^2} \rangle$ and $M_{ij} = \langle \varphi_i, \frac{d^2\varphi_j}{dx^2} \rangle + \langle \frac{d^2\varphi_i}{dx^2}, \varphi_j \rangle$ for each element of the matrices.

Appendix D: Proof of the Convergence Result

Theorem (Convergence of B-spline Approximation). *Let $\Omega = [a, b]$ where $a, b \in \mathbb{R}^+$ and let $g \sim sGP(\alpha, \sigma)$.*

Assume \mathbb{B}_k is a set of k cubic B-splines constructed with equally spaced knots over Ω , and \tilde{g}_k denotes the

corresponding FEM approximation, then:

$$\lim_{k \rightarrow \infty} \mathcal{C}_k(x_1, x_2) = \mathcal{C}(x_1, x_2),$$

for any $x_1, x_2 \in \Omega$, where $\mathcal{C}(x_1, x_2) = \text{Cov}[g(x_1), g(x_2)]$, $\mathcal{C}_k(x_1, x_2) = \text{Cov}[\tilde{g}_k(x_1), \tilde{g}_k(x_2)]$.

Proof. The proof of this theorem starts with a similar strategy as in Lindgren et al. (2011). Without the loss of generality, we assume the variance parameter of the sGP $\sigma = 1$ and $\Omega = [0, 1]$. We denote the 3rd order Sobolev space as $H^3(\Omega) = \{f \in \mathcal{L}^2(\Omega) : D^q f \in \mathcal{L}^2(\Omega) \forall |q| \leq 3\}$. We then define the constrained Sobolev space \mathcal{H} as:

$$\mathcal{H} = \{f \in H^3(\Omega) : f(0) = f'(0) = 0\}.$$

Since $Lf = 0$ implies $f \in \text{span}\{\cos(\alpha x), \sin(\alpha x)\}$, it is clear that

$$\langle f, h \rangle_{\mathcal{H}} := \langle Lf, Lh \rangle_{\Omega} = \int_{\Omega} Lf(x)Lh(x)dx \quad (36)$$

defines an inner product for $f, h \in \mathcal{H}$.

Let $b > 1$ and $\tilde{\Omega} = [0, b) \supset \Omega$, then for each $f \in H^3(\Omega)$, there exists a zero-extension $f_0 \in H^3(\tilde{\Omega})$ such that $f_0(x) = f(x)$ for $x \in \Omega$, and $f_0(b) = f'_0(b) = 0$. Hence, we assume without the loss of generality that for each $f \in \mathcal{H}$, $f(1) = f'(1) = 0$ from now. This implies that the differential operator D^q in \mathcal{H} has adjoint operator $(D^q)^* = (-1)^q D^q$ for each $q \in \mathbb{Z}$.

Define $\mathcal{H}_k = \text{span}\{\mathbb{B}_k\}$. Note $\mathcal{H}_k \subset \mathcal{H}$ by our construction of the B-spline basis. This implies if $f(x) \in \mathcal{H}$, then there exists a projection $\tilde{f}(x) = \sum_{i=1}^k w_i \varphi_i(x) \in \mathcal{H}_k$ which satisfies:

$$\langle f - \tilde{f}, \tilde{h} \rangle_{\mathcal{H}} = \langle f, \tilde{h} \rangle_{\mathcal{H}} - \langle \tilde{f}, \tilde{h} \rangle_{\mathcal{H}} = 0, \quad \forall \tilde{h} \in \mathcal{H}_k. \quad (37)$$

To prove $\lim_{k \rightarrow \infty} \mathcal{C}_k(x_1, x_2) = \mathcal{C}(x_1, x_2)$, note that for any $f, h \in \mathcal{H}$,

$$\begin{aligned}
\text{Cov}[\langle g, f \rangle_{\mathcal{H}}, \langle g, h \rangle_{\mathcal{H}}] &:= \text{Cov}[\langle Lg, Lf \rangle_{\Omega}, \langle Lg, Lh \rangle_{\Omega}] \\
&= \text{Cov}[\langle \xi, Lf \rangle_{\Omega}, \langle \xi, Lh \rangle_{\Omega}] \\
&= \langle Lf, Lh \rangle_{\Omega}, \\
&= \langle f, h \rangle_{\mathcal{H}}.
\end{aligned} \tag{38}$$

The second equality follows from the definition of the sGP, and the third equality follows from the property of Gaussian white noise (Harvey et al., 1990).

Since the B-spline approximation $\tilde{g}_k \in \mathcal{H}_k$, we know

$$\langle \tilde{g}_k, f \rangle_{\mathcal{H}} = \langle \tilde{g}_k, f - \tilde{f} + \tilde{f} \rangle_{\mathcal{H}} = \langle \tilde{g}_k, \tilde{f} \rangle_{\mathcal{H}} + \langle \tilde{g}_k, f - \tilde{f} \rangle_{\mathcal{H}} = \langle \tilde{g}_k, \tilde{f} \rangle_{\mathcal{H}}.$$

Using this result and the fact that the B-spline approximation \tilde{g}_k is a least square solution, we have

$$\begin{aligned}
\text{Cov} \left[\langle \tilde{g}_k, f \rangle_{\mathcal{H}}, \langle \tilde{g}_k, h \rangle_{\mathcal{H}} \right] &= \text{Cov} \left[\langle \tilde{g}_k, \tilde{f} \rangle_{\mathcal{H}}, \langle \tilde{g}_k, \tilde{h} \rangle_{\mathcal{H}} \right] \\
&= \text{Cov} \left[\langle \xi, L\tilde{f} \rangle_{\Omega}, \langle \xi, L\tilde{h} \rangle_{\Omega} \right] \\
&= \langle \tilde{f}, \tilde{h} \rangle_{\mathcal{H}}.
\end{aligned} \tag{39}$$

Let $\mathcal{C}_s(x) = \mathcal{C}(s, x)$ denote the covariance function of the sGP defined at any $s \in \Omega$. Based on the previous result in Proposition 1, we know $\mathcal{C}_s(x) \in \mathcal{H}$ and $L\mathcal{C}_s(x) = \frac{1}{\alpha} \sin[\alpha(s-x)^+]$ is the Green function of L . Its projection into \mathcal{H}_k is denoted as $\tilde{\mathcal{C}}_s(x)$

Lemma 1. *Given the same setting in the main theorem*

$$\begin{aligned}
\mathcal{C}(x_1, x_2) &= \text{Cov}[\langle g, \mathcal{C}_{x_1} \rangle_{\mathcal{H}}, \langle g, \mathcal{C}_{x_2} \rangle_{\mathcal{H}}] \\
\mathcal{C}_k(x_1, x_2) &= \text{Cov} \left[\langle \tilde{g}_k, \tilde{\mathcal{C}}_{x_1} \rangle_{\mathcal{H}}, \langle \tilde{g}_k, \tilde{\mathcal{C}}_{x_2} \rangle_{\mathcal{H}} \right].
\end{aligned} \tag{40}$$

Proof. The first part directly follows from the proof in Proposition 1. The second part can be proved using the fact that L is self-adjoint and $L\mathcal{C}_{x_1}(x) = \frac{1}{a} \sin[a(x_1-x)^+]$ is the Green function, which implies $\langle \varphi_i, \tilde{\mathcal{C}}_{x_1} \rangle_{\mathcal{H}} = \varphi_i(x_1)$ for each $i \in [k]$. The detailed proof proceeds as the following.

By construction of the B-spline approximation,

$$\begin{aligned}
\mathcal{C}_k(x_1, x_2) &= \text{Cov} \left[\sum_i w_i \varphi_i(x_1), \sum_i w_i \varphi_i(x_2) \right] \\
&= \text{Cov} \left[\mathbf{\Phi}(x_1)^T \mathbf{w}, \mathbf{\Phi}(x_2)^T \mathbf{w} \right] \\
&= \mathbf{\Phi}(x_1)^T \Sigma_{\mathbf{w}} \mathbf{\Phi}(x_2),
\end{aligned} \tag{41}$$

where $\mathbf{\Phi}(x) = [\varphi_1(x), \dots, \varphi_k(x)]^T$.

Since $\tilde{\mathcal{C}}_{x_1}(x)$ is the projection of $\mathcal{C}_{x_1}(x)$ to \mathcal{H}_k , $\tilde{\mathcal{C}}_{x_1}(x) = \sum_i w_{x_1, i} \varphi_i(x)$ for some weights $\mathbf{w}_{x_1} = [w_{x_1, 1}, \dots, w_{x_1, k}]^T$.

The same argument can be used for $\tilde{\mathcal{C}}_{x_2}$. Therefore

$$\begin{aligned}
\text{Cov} \left[\left\langle \tilde{g}_k, \tilde{\mathcal{C}}_{x_1} \right\rangle_{\mathcal{H}}, \left\langle \tilde{g}_k, \tilde{\mathcal{C}}_{x_2} \right\rangle_{\mathcal{H}} \right] &= \left\langle \tilde{\mathcal{C}}_{x_1}, \tilde{\mathcal{C}}_{x_2} \right\rangle_{\mathcal{H}} \\
&= \left\langle \mathbf{\Phi}(x)^T \mathbf{w}_{x_1}, \mathbf{\Phi}(x)^T \mathbf{w}_{x_2} \right\rangle_{\mathcal{H}} \\
&= \left\langle L \mathbf{\Phi}(x)^T \mathbf{w}_{x_1}, L \mathbf{\Phi}(x)^T \mathbf{w}_{x_2} \right\rangle_{\Omega} \\
&= \mathbf{w}_{x_1}^T \Sigma_{\mathbf{w}}^{-1} \mathbf{w}_{x_2}.
\end{aligned} \tag{42}$$

Solving $\left\langle \tilde{\mathcal{C}}_{x_1}, \varphi_i \right\rangle_{\mathcal{H}} = \left\langle \mathcal{C}_{x_1}, \varphi_i \right\rangle_{\mathcal{H}}$ for each $i \in [k]$ yields that $\mathbf{w}_{x_1} = \Sigma_{\mathbf{w}} \boldsymbol{\omega}_{x_1}$, where $\boldsymbol{\omega}_{x_1} \in \mathbb{R}^k$ with i th element $\omega_{x_1, i} = \left\langle \mathcal{C}_{x_1}, \varphi_i \right\rangle_{\mathcal{H}}$. Hence it only remains to show $\boldsymbol{\omega}_{x_1} = \mathbf{\Phi}(x_1)$, which holds because

$$\begin{aligned}
\omega_{x_1, i} &= \left\langle \mathcal{C}_{x_1}, \varphi_i \right\rangle_{\mathcal{H}} \\
&= \left\langle L \mathcal{C}_{x_1}, L \varphi_i \right\rangle_{\Omega} \\
&= \left\langle L^* L \mathcal{C}_{x_1}, \varphi_i \right\rangle_{\Omega} \\
&= \varphi_i(x_1), \quad \forall i \in [k].
\end{aligned} \tag{43}$$

The last equality holds because L is a self-adjoint operator and $L \mathcal{C}_{x_1}$ is the Green function. This lemma is hence proved. \square

Using the above result and Lemma 1, it suffices to prove that

$$\left\langle \tilde{\mathcal{C}}_{x_1}, \tilde{\mathcal{C}}_{x_2} \right\rangle_{\mathcal{H}} \rightarrow \left\langle \mathcal{C}_{x_1}, \mathcal{C}_{x_2} \right\rangle_{\mathcal{H}}, \tag{44}$$

as $k \rightarrow \infty$. For this step, we will use the following lemma on the spline approximation:

Lemma 2. *Given the same setting in the main theorem, define the norm $\|f\|_{\mathcal{H}} = \langle f, f \rangle_{\mathcal{H}}^{1/2}$ for $f \in \mathcal{H}$ then*

$$\|\mathcal{C}_s - \tilde{\mathcal{C}}_s\|_{\mathcal{H}} = O(1/k), \quad (45)$$

for each $s \in \Omega$.

Proof. The proof of this lemma mostly follows from the result in Schultz (1969). Given \mathcal{H}_k is a spline space with degree 3 and mesh size $1/k$ and $\mathcal{C}_s \in H^3(\Omega)$, by theorem 3.3 in Schultz (1969) we have

$$\|D^q(\mathcal{C}_s - \tilde{\mathcal{C}}_s)\|_{H^2(\Omega)} \leq c_q \left(\frac{1}{k}\right)^{3-q} \quad (46)$$

for each $0 \leq q \leq 2$, where c_q is a constant that depends on $\|\mathcal{C}_s\|_{H^3(\Omega)}$ but does not depend on k . Note that

$$\begin{aligned} \|\mathcal{C}_s - \tilde{\mathcal{C}}_s\|_{\mathcal{H}}^2 &= \alpha^4 \|\mathcal{C}_s - \tilde{\mathcal{C}}_s\|_{\mathcal{L}^2}^2 + \|D^2(\mathcal{C}_s - \tilde{\mathcal{C}}_s)\|_{\mathcal{L}^2}^2 - 2\alpha \left\langle (\mathcal{C}_s - \tilde{\mathcal{C}}_s), D^2(\mathcal{C}_s - \tilde{\mathcal{C}}_s) \right\rangle_{\Omega} \\ &= \alpha^4 \|\mathcal{C}_s - \tilde{\mathcal{C}}_s\|_{\mathcal{L}^2}^2 + \|D^2(\mathcal{C}_s - \tilde{\mathcal{C}}_s)\|_{\mathcal{L}^2}^2 + 2\alpha \|D(\mathcal{C}_s - \tilde{\mathcal{C}}_s)\|_{\mathcal{L}^2}^2, \end{aligned} \quad (47)$$

where the second equality holds since $D^* = -D$. The lemma is proved since $\|\cdot\|_{\mathcal{H}}$ and $\|\cdot\|_{H^2(\Omega)}$ are equivalent norm. □

Using Lemma 2, Eq. (44) can be proved with Cauchy Schwarz inequality and the fact that the sequence

$\|\tilde{\mathcal{C}}_{x_2}\|_{\mathcal{H}}$ is bounded,

$$\begin{aligned} \left| \left\langle \tilde{\mathcal{C}}_{x_1}, \tilde{\mathcal{C}}_{x_2} \right\rangle_{\mathcal{H}} - \langle \mathcal{C}_{x_1}, \mathcal{C}_{x_2} \rangle_{\mathcal{H}} \right| &= \left| \left\langle \tilde{\mathcal{C}}_{x_1} - \mathcal{C}_{x_1}, \tilde{\mathcal{C}}_{x_2} \right\rangle_{\mathcal{H}} - \left\langle \mathcal{C}_{x_1}, \mathcal{C}_{x_2} - \tilde{\mathcal{C}}_{x_2} \right\rangle_{\mathcal{H}} \right| \\ &\leq \|\tilde{\mathcal{C}}_{x_1} - \mathcal{C}_{x_1}\|_{\mathcal{H}} \|\tilde{\mathcal{C}}_{x_2}\|_{\mathcal{H}} + \|\tilde{\mathcal{C}}_{x_2} - \mathcal{C}_{x_2}\|_{\mathcal{H}} \|\mathcal{C}_{x_1}\|_{\mathcal{H}} \\ &= c/k, \end{aligned} \quad (48)$$

where c is some constant independent of k . The theorem is hence proved. □